

Discovery of a Gas Giant Planet in Microlensing Event OGLE-2014-BLG-1760

A. Bhattacharya^{1,M}, D.P. Bennett^{1,2,M}, I.A. Bond^{3,M}, T. Sumi^{4,M}, A. Udalski^{5,O}, R. Street^{6,R},
Y. Tsapras^{6,7,8,R}

and

F. Abe⁹, M. Freeman¹⁰, A. Fukui¹¹, Y. Itow⁹, M. C. A. Li¹², C. H. Ling³, K. Masuda⁹,
Y. Matsubara⁹, Y. Muraki⁹, K. Ohnishi¹³, L. C. Philpott¹⁴, N. Rattenbury¹², T. Saito¹⁵,
A. Sharan¹², D. J. Sullivan¹⁶, D. Suzuki², P. J. Tristram¹⁷

(*MOA* collaboration),

J. Skowron⁵, M. K. Szymański⁵, I. Soszyński⁵, R. Poleski^{5,18}, P. Mróz⁵, S. Kozłowski⁵,
P. Pietrukowicz⁵, K. Ulaczyk⁵, L. Wyrzykowski⁵

(*OGLE* collaboration),

E. Bachelet^{6,19}, D. M. Bramich^{19,20}, G. D'Agostino^{21,22}, M. Dominik^{23,†}, R. Figuera Jaimes^{20,23},
K. Horne²³, M. Hundertmark^{24,25}, N. Kains²⁶, J. Menzies²⁷, R. Schmidt⁷,
C. Snodgrass^{28,29}, I. A. Steele³⁰, J. Wambsganss⁷

(*ROBONET* collaboration)

ABSTRACT

We present the analysis of the planetary microlensing event OGLE-2014-BLG-1760, which shows a strong light curve signal due to the presence of a Jupiter mass-ratio planet. One unusual feature of this event is that the source star is quite blue, with $V - I = 1.48 \pm 0.08$. This is marginally consistent with source star in the Galactic bulge, but it could possibly indicate a young source star in the far side of the disk. Assuming a bulge source, we perform a Bayesian analysis assuming a standard Galactic model, and this indicates that the planetary system resides in or near the Galactic bulge

¹Department of Physics, University of Notre Dame, 225 Nieuwland Science Hall, Notre Dame, IN 46556, USA;
Email: abhata2@nd.edu

²Code 667, NASA Goddard Space Flight Center, Greenbelt, MD 20771, USA

³Institute of Natural and Mathematical Sciences, Massey University, Auckland 0745, New Zealand

⁴Osaka University, 1-1 Yamadaoka, Suita, Osaka Prefecture 565-0871, Japan

⁵Warsaw University Observatory, Al. Ujazdowskie 4, 00-478 Warszawa, Poland

⁶Las Cumbres Observatory Global Telescope Network, 6740 Cortona Drive, Suite 102, Goleta, CA 93117, USA

⁷Astronomisches Rechen-Institut, Zentrum für Astronomie der Universität Heidelberg (ZAH), 69120 Heidelberg, Germany

⁸School of Physics and Astronomy, Queen Mary University of London, Mile End Road, London E1 4NS, UK

⁹Institute for Space-Earth Environmental Research, Nagoya University, 464-8601 Nagoya, Japan

¹⁰Dept of Physics, University of Auckland, Private Bag 92019, Auckland, New Zealand

¹¹Okayama Astrophysical Observatory, National Astronomical Observatory of Japan, Asakuchi, 719-0232 Okayama, Japan

¹²Dept. of Physics, University of Auckland, Private Bag 92019, Auckland, New Zealand

¹³Nagano National College of Technology, 381-8550 Nagano, Japan

¹⁴Department of Earth, Ocean and Atmospheric Sciences, University of British Columbia, Vancouver, British Columbia, Vancouver, British Columbia, V6T 1Z4, Canada

¹⁵Tokyo Metropolitan College of Industrial Technology, 116-8523 Tokyo, Japan

¹⁶School of Chemical and Physical Sciences, Victoria University, Wellington, New Zealand

¹⁷Mt. John University Observatory, P.O. Box 56, Lake Tekapo 8770, New Zealand

¹⁸Department of Astronomy, Ohio State University, 140 West 18th Avenue, Columbus, OH 43210, USA

¹⁹Qatar Environment and Energy Research Institute (QEERI), HBKU, Qatar Foundation, Doha, Qatar

²⁰European Southern Observatory, Karl-Schwarzschild-Str. 2, 85748 Garching bei München, Germany

²¹Dipartimento di Fisica “E.R. Caianiello”, Università di Salerno, Via Ponte Don Melillo, 84084-Fisciano (SA), Italy

²²Istituto Nazionale di Fisica Nucleare, Sezione di Napoli, Napoli, Italy

²³School of Physics & Astronomy, University of St Andrews, North Haugh, St Andrews KY 16 9SS, UK

²⁴Niels Bohr Institute, University of Copenhagen, Juliane Maries Vej 30, 2100, Kobenhavn, Denmark

²⁵SUPA, School of Physics & Astronomy, University of St Andrews, North Haugh, St Andrews KY16 9SS, UK

²⁶Space Telescope Institute, 3700 San Martin Drive, Baltimore, MD 21218, USA

²⁷South African Astronomical Observatory, PO Box 9, Observatory 7935, South Africa

²⁸Planetary and Space Sciences, Dept of Physical Sciences, The Open University, Milton Keynes, MK7 6AA, UK

²⁹Max Planck Institute for Solar System Research, Justus-von-Liebig-Weg 3, 37077 Göttingen, Germany

³⁰Astrophysics Research Institute Liverpool John Moores University, Liverpool L3 5RF, UK and Royal Society University Research Fellow

[†]Royal Society University Research Fellow

^MMicrolensing Observation in Astrophysics

^OOptical Gravitational Lensing Experiment

^RRobonet

at $D_L = 6.9 \pm 1.1$ kpc. It also indicates a host star mass of $M_* = 0.51 \pm 0.44 M_\odot$, a planet mass of $m_p = 180 \pm 110 M_\oplus$, and a projected star-planet separation of $a_\perp = 1.7 \pm 0.3$ AU. The lens-source relative proper motion is $\mu_{\text{rel}} = 6.5 \pm 1.1$ mas/yr. The lens (and stellar host star) is predicted to be very faint, so it is most likely that it can be detected only when the lens and source stars are partially resolved. Due to the relatively high relative proper motion, the lens and source will be resolved to about ~ 46 mas in 6-8 years after the peak magnification. So, by 2020 - 2022, we can hope to detect the lens star with deep, high resolution images.

Subject headings: gravitational lensing: micro, planetary systems

1. Introduction

Gravitational Microlensing is the technique of detecting exoplanets using gravitational lensing. Microlensing is unique in its ability to detect planets (Gould & Loeb 1992) just outside of the snow line (Lissauer 1993) down to an earth mass (Bennett & Rhie 1996), which is difficult or impossible with other methods. According to the core accretion theory, the snow line (Ida & Lin 2005; Lecar et al. 2006; Kennedy et al. 2006; Kenyon & Hartmann 1995) plays a very crucial role in the planet formation process. Beyond the snow line, ices condense, increasing the density of the solid materials. Higher density of solids speeds the planet formation process in the protoplanetary disk, hence forming cold planets quickly beyond the snow line. The planets, discovered by microlensing, provide the statistics needed to understand the architecture of cold planets beyond the snow line (Suzuki et al. 2016). Since this method does not rely on the light from the host stars, it can detect planets, even when the host stars cannot be detected (Mao & Paczyński 1991). Most of the planets discovered so far using microlensing are $\sim 1-8$ kpc away. Thus, microlensing is able to detect planets in the inner Galactic disk and bulge, where it is difficult to detect planets with other methods. Thus, microlensing has the potential to measure how the properties of exoplanets depend on the Galactic environment.

For most planetary microlensing events, the angular Einstein radius, θ_E is measured from the finite source effect. In events where the lens star brightness (Bennett et al. 2006) or the parallax effect is measured (Gould 1992; Gaudi et al. 2008; Muraki et al. 2011), the planetary mass and distance to the planetary system can be determined. Hence this technique can be used to build statistics of planetary mass as a function of the host star mass. Since the planets detected by microlensing are $\sim 1-8$ kpc away, the distance to the planetary system will also allow the determination of the planetary mass function as a function of the distance towards the galactic center.

In this paper we present the discovery of a gas giant planet orbiting the lens stars for microlensing event OGLE-2014-BLG-1760. The mass ratio of this planet is $q = 8.64 \times 10^{-4}$, which is slightly less than that of Jupiter. The paper is organized as follows: Section 2 describes the light

curve data collected for the event OGLE-2014-BLG-1760. The next section (Section 3) is divided in four parts: 3.1 summarizes data reduction procedures for the different data sets; Section 3.2 shows the best fit model and procedures that are used to obtain it; Section 3.3 describes how the limb darkening of the source is modeled; and section 3.4 presents our attempt to detect the microlensing parallax effect in the light curve. In Section 4, we discuss source brightness and angular radius measurement and derive the lens-source relative proper motion. Section 5 discusses an estimate of the lens properties and the future possible investigations.

2. Observation

The *OGLE* (Optical Gravitational Lensing Experiment) collaboration operates a microlensing survey towards the galactic bulge, with the 1.3 meter Warsaw telescope from Las Campanas observatory in Chile. Most of the OGLE-IV (phase 4) observations were taken in the Cousins *I*-band, with occasional observations in Johnson *V*-band (Udalski et al. 2015). In the year 2014, OGLE Early Warning System (EWS) (Udalski et al. 1994) has alerted 2049 microlensing candidates of which this event OGLE-2014-BLG-1760 was the 1760th one.

The *MOA* (Microlensing Observation in Astrophysics) (Bond et al. 2001) collaboration also operates a microlensing survey towards the galactic bulge with the 1.8 meter MOA-II telescope from Mount John Observatory at Lake Tekapo, New Zealand. The observations are mostly taken in MOA-red wide band filter which covers the wavelengths of the standard Cousins *R* + *I* bands. For year 2014, MOA has reported about ~ 33 microlensing anomalies out of which OGLE-2014-BLG-1760 planetary event is one of them.

Both of these telescopes have relatively large fields-of-view, 2.2 deg^2 for MOA-II, and 1.4 deg^2 for OGLE-IV. These enable survey observations with cadences as high as one observation every 15 minutes, and this allows the surveys to detect the sharp light curve features of planetary light curve features, when they are only smoothed by the finite source effects of a main sequence source star. It is the high cadence observation of microlensing events of MOA-II and OGLE-IV survey that helps in detecting microlensing anomalies, including the microlensing planetary signatures.

The microlensing event OGLE-2014-BLG-1760 was discovered at (RA,decl.)(2000) = (17 : 57 : 38.16, $-28 : 57 : 47.37$)[(l,b)=(1.3186, -2.2746)], by the OGLE EWS on August 22, 2014 around 7.25 a.m. EDT. The same event was alerted by MOA on August 31, 2014 as MOA-2014-BLG-547. Later, on September 10, 2014, the MOA collaboration detected the planetary cusp crossing and announced the anomaly in the light curve (around HJD = 2456911 in Figure 1). In response to MOA anomaly alert, the follow up groups Robonet and μ FUN started collecting data on this event. The high cadence observation of MOA-II survey covered most of the cusp crossing, and the trough after the cusp crossing was well covered by follow up groups, Robonet and μ FUN. The Robonet group observed the event with 1 m robotic telescopes at Cape Town, South Africa and at Siding Springs, Australia, in the Sloan *I*-band. The μ FUN group also observed the event with the 1.3 m

SMARTS CTIO telescopes in both the V and I -bands. All these observations are shown in Figure 1. Although the μ FUN data is pretty flat because the trough is followed by the normal single lens decrease (see Figure 1), the μ FUN data do help to exclude the wide model with $s = 1.27$ and contribute in constraining the planetary model (discussed in section 3.2). It is true that the constraint from the Robonet and OGLE data is stronger because of better Robonet coverage and OGLE observations over a wider range of magnifications.

3. Data Reduction and Modeling

3.1. Data Reduction

All the images were reduced to photometry using the difference image method (Tomany & Crofts 1996; Alard & Lupton 1998; Alard 2000). The MOA images were reduced using MOA difference image analysis pipeline (Bond et al. (2001)). The data was then detrended using the non-2014 data to minimize the error due to the effects of differential refraction, seeing and airmass. To avoid systematic errors due to flat field changes and changes in detector sensitivity, we removed data prior to 2011 and only use the data after $HJD' = 5596$ (February, 2011) for modeling. OGLE data were reduced using OGLE Difference Image Analysis software and optimal centroid method (Udalski (2003); Wozniak (2000)). The μ FUN photometry was produced using a modified version of the PySIS package (Albrow et. al. 2009). Robonet data were reduced using the DanDIA package Bramich (2008).

The error bar estimates obtained from the photometry codes are sufficient to find the best fit model. These error bar estimates are good measures of the relative uncertainties for measurements with the same telescope, but they are often wrong by a factor of ~ 2 . To determine the uncertainties for the model parameters, it is necessary to have accurate error bars which will give $\chi^2/\text{dof} \approx 1$ for each passband. We used method of Bennett et al. (2014) to normalize the error bars using $\sigma'_i = k\sqrt{\sigma_i^2 + e_{min}^2}$. Here σ_i is the initial uncertainty of i -th data point; σ'_i is the modified error bar. A k value is selected for each passband to give $\chi^2/\text{dof} = 1$. Our initial fits used $k = 1.50$ and $e_{min} = 0.003$ for all passbands. Next, once the best fit model was found, the values of k was modified for each passband to satisfy $\chi^2/\text{dof} = 1$. The number of datapoints used for each passband and their corresponding k values are listed in Table 1. New fits were done with the new error bars, which resulted in very small changes to the model parameters.

3.2. Best Fit Model

We begin our modeling of the OGLE-2014-BLG-1760 light curve with single lens microlensing model (Paczynski 1986). There are three non-linear model parameters for a single lens event: t_0 - the time of peak magnification, u_0 - the minimum separation between source and lens in Einstein

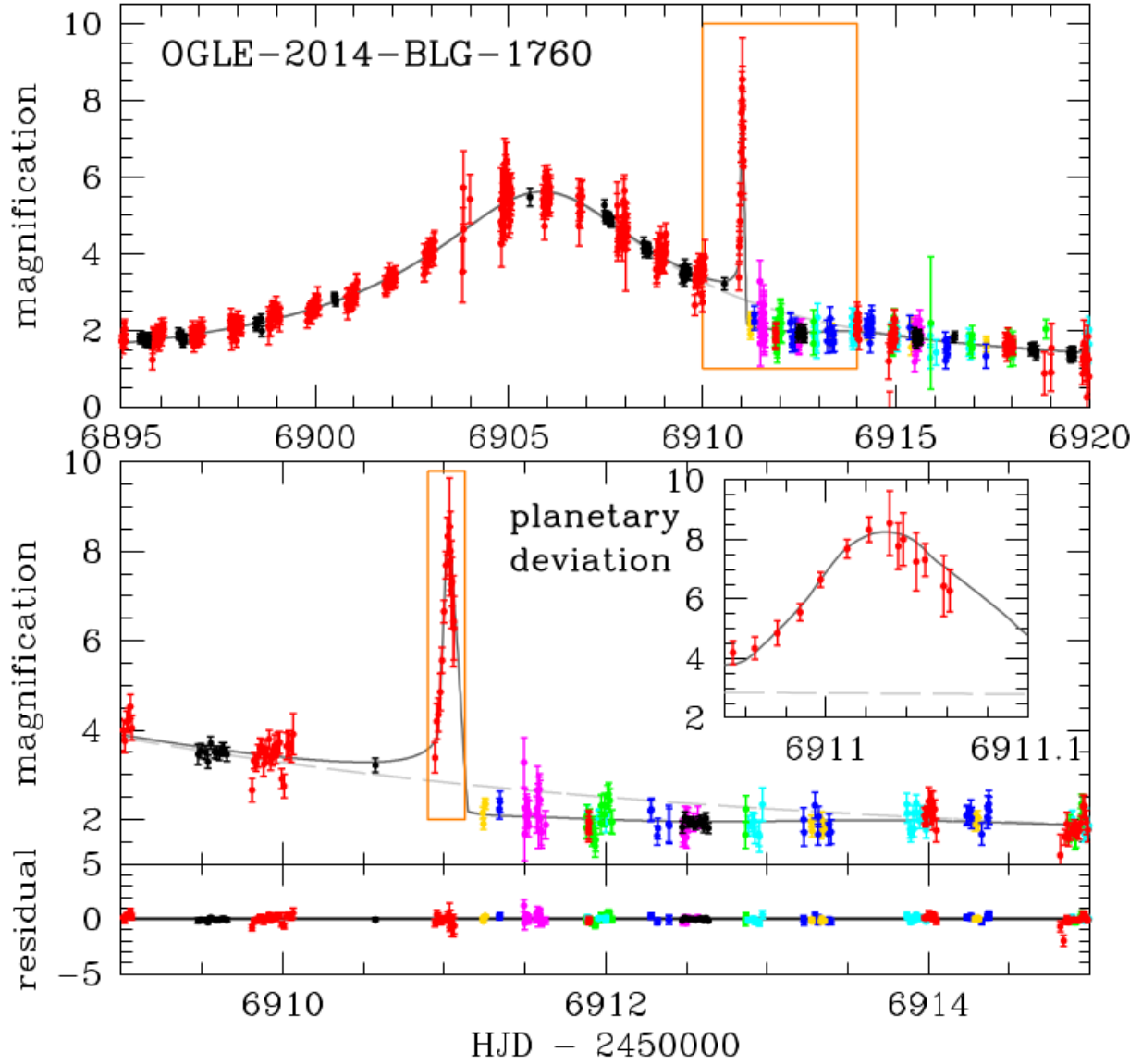


Fig. 1.— The light curve of event OGLE-2014-BLG-1760. The light grey dashed line represent the best fit single lens model and the dark grey line represents the best planetary model. The data are plotted in the following colors: red for the MOA-red band, black for OGLE-*I*, purple for OGLE-*V*, (difficult to see due to overlap with the OGLE-*I* data), blue for the ROBONET SAAO-A *I*-band, gold for the ROBONET SAAO-B *I*-band, green for the ROBONET Siding Springs-A *I*-band, cyan for the ROBONET Siding Springs-B *I*-band, and magenta for the μ FUN *I*-band.

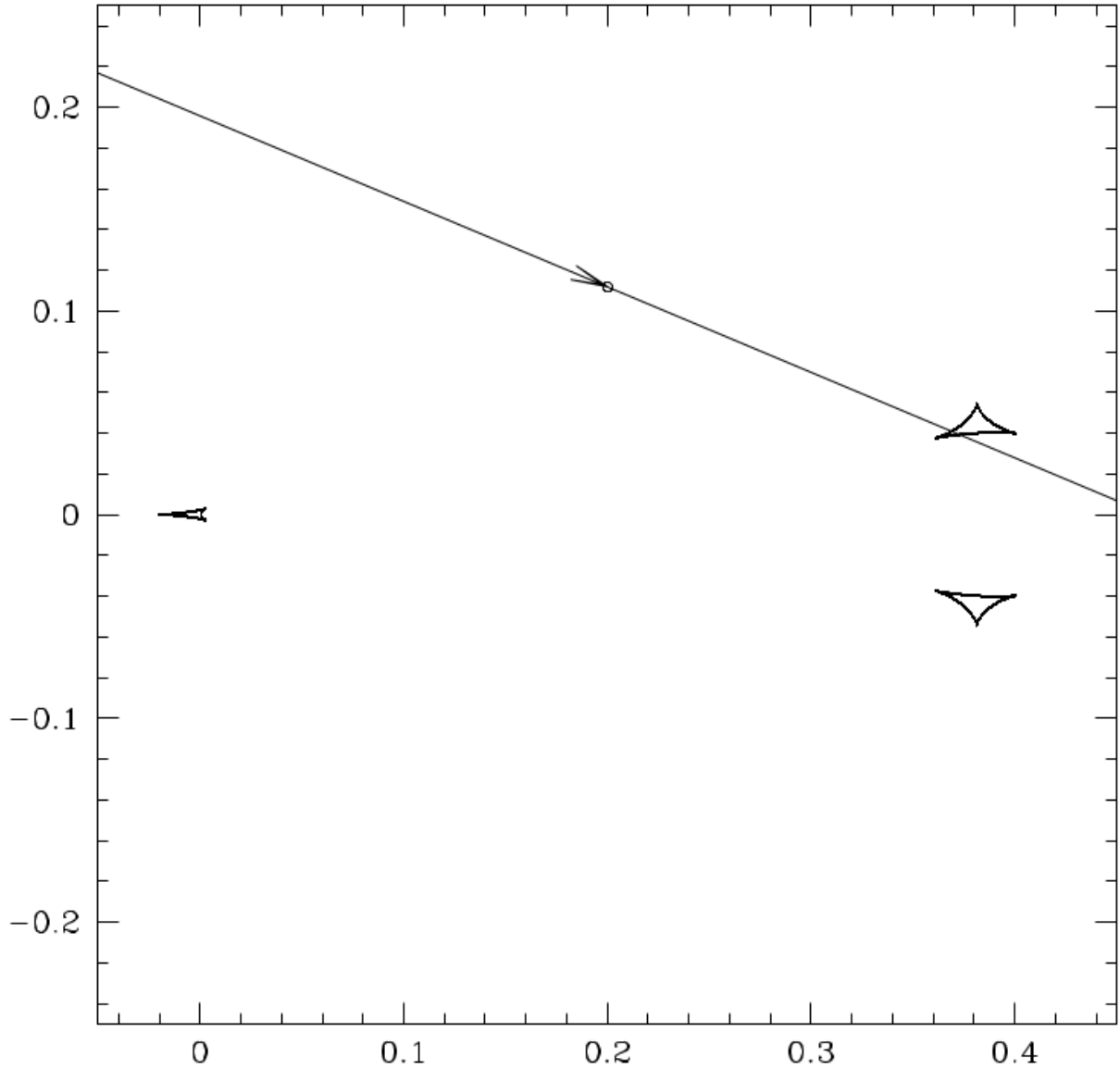


Fig. 2.— This figure shows the caustic configuration and source trajectory for the best fit planetary model. When the source crosses inside the planetary caustic, its magnification jumps as two new highly magnified images are created, and then the magnification drops just as abruptly when the source exits and two images disappear. The two caustic crossings are at $\text{HJD}' - 2450000 = 6911.00$ and 6911.07 . Since the interval between the caustic crossings is similar to the source radius crossing time, t_* , the two magnification peaks merge into one peak, as shown in Figure 1 at $\text{HJD}' \sim 6911$. Also, when the source passes between the two minor image planetary caustics, the magnification of the source brightness drops, as can be seen in the light curve after caustic crossing, between $\text{HJD}' = 6911.20$ and 6914.00 in Figure 1.

radius units, and t_E - the Einstein radius crossing time. There are also two linear parameters for each passband: the source flux f_s , and the blend flux, f_{bl} . We find the best single lens parameters as the starting point for a systematic search through parameter space to find the best binary lens solution. Because the light curve follows a single lens shape for most of its history, except in the vicinity of the planetary feature at $t \approx 6911$, we can use the best fit single lens parameters as the starting point for an initial condition grid search, following Bennett (2010).

To describe a binary lens, we need three additional parameters: the lens mass ratio, q , the projected separation between the lens masses, s , measured in Einstein radius units, and the angle between the source trajectory and the lens axis, θ . Also, binary events often have caustic or cusp crossings, which resolve the angular size of the source, so we need an additional parameter, the source radius crossing time, t_* , to model finite source effects. With the single lens parameters fixed to the best fit values, we use the initial condition grid search method to search over the parameter ranges $0.48 \leq s \leq 2.10$, $-4 \leq \log q \leq -2$, and $-\pi \leq \theta \leq \pi$, with t_* fixed at $t_* = 0.05$. We then select ~ 10 of the best fit values from the initial condition grid search (with very different values of q , s and θ) to use as initial conditions for full, non-linear modeling runs using the Bennett (2010) χ^2 minimization recipe, which is a modification of Markov Chain Monte Carlo algorithm (Verde et al. 2003). The parameters of the best fit binary lens model and the χ^2 improvement are compared with the best fit single lens model in Table 2. The binary lens best fit model has $q = 8.64 \times 10^{-4}$ improves the renormalized χ^2 by $\Delta\chi^2 = 1218.75$ compared to the best fit single lens model. Hence the binary lens model is the preferred model.

High magnification planetary microlensing events usually have a “close-wide” degeneracy, in

Table 1. Data Reduction Summary

Telescope	Filter	N^a/N^b	k
MOA	red(I+R)	11655/11673	0.63
OGLE	I	10779/10794	0.98
OGLE	V	119/119	0.84
μ FUN	I	45/45	0.79
μ FUN	V	3/4	0.99
ROBONET SAAO A	I	54/54	1.16
ROBONET SAAO B	I	32/32	0.96
ROBONET Siding springs- A	I	56/56	1.24
ROBONET Siding springs- B	I	75/75	1.23

^a Number of data points used

^b Number of total observations

that solutions with $s \leftrightarrow 1/s$ are nearly degenerate. This is usually not the case for low magnification planetary events because the caustic structure for the major and minor image caustics is quite different. However, the major and minor image caustics with $s \leftrightarrow 1/s$ are encountered at the same single lens magnification, and with specific source trajectories, it is possible to produce similar light curves with both $s > 1$ and $s < 1$, particularly if the light curves aren't very well sampled. Therefore, we have searched for models with $s \sim 1/0.83 = 1.20$. We found a best fit $s > 1$ model with $s = 1.27$, but this is a worse fit than the best fit model (with $s = 0.83$) by $\Delta\chi^2 \sim 215$. This is because the OGLE-2014-BLG-1760 is well sampled, so the $s = 1.27$ model is excluded, and the $s = 0.83$ is the only viable solution.

3.3. Limb Darkening Effect

The photometric calibrations and the extinction toward the red clump stars in the vicinity of the source are discussed in Section 4. The magnitude and color of the source are indicated with the cyan point in Figure 4, and the extinction corrected color is $(V - I)_{S,0} = 0.34$, as discussed in section 4. This color implies that the source is an \sim A9 star with $T_{\text{eff}} \sim 7352$ K from Kenyon & Hartmann (1995). We use a linear limb darkening model, and from Claret (2000), we select the limb darkening parameters u to be 0.4204, 0.5790 and 0.46035 corresponding to the V , I and MOA-Red bands, respectively. These corresponds to the temperature of $T_{\text{eff}} = 7352$ K and a surface gravity of $\log g = 4.5$. The parameters of the best fit model are insensitive to the precise limb darkening parameters.

3.4. Search for a Microlensing Parallax Signal

The microlensing parallax effect has been detected in a number of planetary microlensing events (Gaudi et al. 2008; Bennett et al. 2010; Muraki et al. 2011) where it has allowed the lens system masses to be measured. Due to the Earth's orbital motion about the Sun, the apparent lens - source relative motion deviates from uniform linear motion. This phenomenon is known as microlensing parallax effect (Gould 1992; Alcock et. al. 1995). The parallax effect can be described with the parallax vector $\boldsymbol{\pi}_E = (\pi_{E,N}, \pi_{E,E})$, where direction of $\boldsymbol{\pi}_E$ is same as lens-source relative proper motion, μ_{rel} . The amplitude of π_E is the inverse of the Einstein radius projected to the observer's plane, $\pi_E = \text{AU}/\tilde{r}_E$. When both the microlensing parallax effect and the angular Einstein radius (as described in section 4) are measured, we can determine the lens system mass and distance from the following equations:

$$M_L = \frac{\theta_E}{k\pi_E} \quad (1)$$

$$D_L = \frac{\text{AU}}{\pi_E\theta_E + \frac{\text{AU}}{D_S}} \quad (2)$$

where $k = 4G/(c^2\text{AU}) = 8.14 \text{ mas } M_\odot^{-1}$, M_L is the total mass of host star and planet and D_L and $D_S \sim 8 \text{ kpc}$ are the distances to the lens system and source stars, respectively. The host star mass, M_* , is given by $M_* = M_L/(1 + q)$.

In order to include the microlensing parallax effect, we must add two new model parameters π_E and ϕ_E , the magnitude and direction angle of the parallax vector. (The north and east components of $\boldsymbol{\pi}_E$ are given by $\pi_{E,N} = \pi_E \cos(\phi_E)$ and $\pi_{E,E} = \pi_E \sin(\phi_E)$.) Our best fit parallax model has an unusually large π_E value of $\pi_E = 5.86$, which would imply a very nearby and low mass lens if it is an accurate measurement, but the improvement in χ^2 is only $\Delta\chi^2 = 9.90$ over the best fit without parallax. We can examine the origins of this parallax signal by examining the cumulative $\Delta\chi^2$ between the non-parallax and parallax models as a function of time, which we show in Figure 3. The cumulative $\Delta\chi^2$ is displayed for the MOA and OGLE data separately, and we can see that only the OGLE data favors the parallax model. Penny et al. (2016) consider the distribution of published planetary microlensing events and show there are an implausibly large number with “high” microlensing parallax values ($\pi_E \gtrsim 1$). This suggests that some of the published planetary events have spurious large π_E values (Han et al. 2016). We conclude that this microlensing parallax measurement for OGLE-2014-BLG-1760 is also spurious.

4. Calibration and Source Properties

The OGLE data were taken in the OGLE-IV I and V -bands, which we calibrate to the OGLE-III catalog Cousins I and Johnson V band (Szymański et al. 2010). 151 bright ($I \leq 16.50$) and isolated stars were matched in both passbands and used for this calibration. The following calibration relations are used to convert OGLE VI magnitudes to OGLE III Catalog Cousins I and Johnson V magnitude:

Table 2. Model Parameters

parameter	units	binary lens best fit	single lens best fit
t_E	days	15.87 ± 0.41	15.47
t_0	HJD-2450000	6905.856 ± 0.026	6905.9541
u_0		0.1806 ± 0.0074	0.19
s		0.8269 ± 0.0047	
θ	radian	-0.3977 ± 0.0086	
q	10^{-4}	8.64 ± 0.89	
t_*	days	0.0366 ± 0.0044	
fit χ^2		22818.05	24036.80

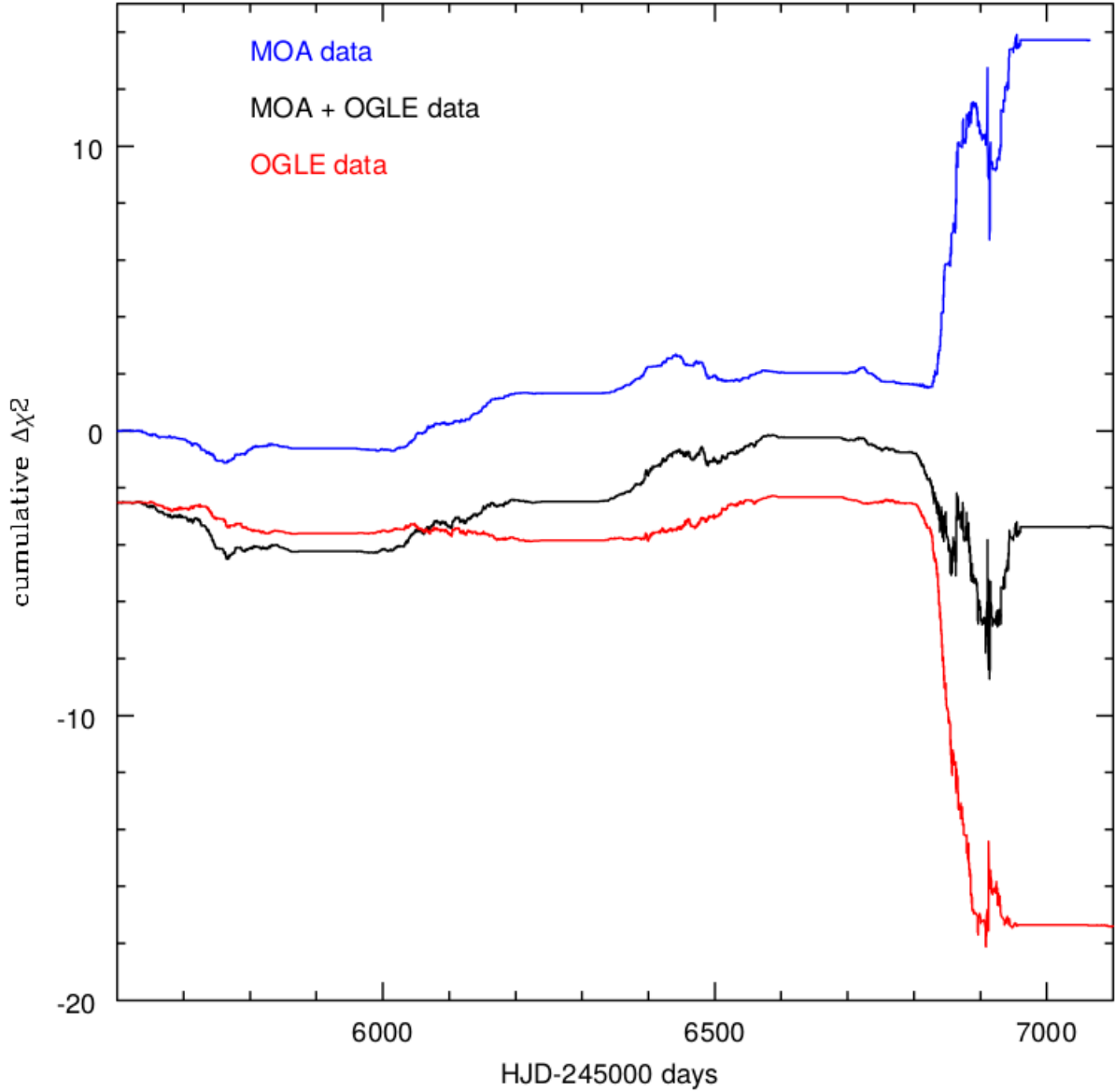


Fig. 3.— The difference in the cumulative χ^2 values between the best fit models with and without parallax are shown for MOA data (blue), OGLE data (red) and total MOA + OGLE data (black). The negative cumulative $\Delta\chi^2$ means parallax model is supported. Also MOA data does not support parallax whereas OGLE data supports parallax model. The χ^2 improvement from MOA + OGLE data for parallax model is ~ 3.60 . The overall χ^2 improvement for parallax model from all the telescopes is ~ 9.90 . Hence the parallax signal is dubious and probably a false signal.

$$I_{\text{OGLEIV}} = -0.0471 + 0.99867I_{\text{OGLEIII}} + 0.00133V_{\text{OGLEIII}} \quad (3)$$

$$V_{\text{OGLEIV}} = -0.3444 - 0.10068I_{\text{OGLEIII}} + 1.10068V_{\text{OGLEIII}} \quad (4)$$

The uncertainty in the brightness due to these calibration relations is ~ 0.01 magnitude. The source brightness in the OGLE III catalog scale is $I_S = 19.07 \pm 0.14$, $V_S = 20.51 \pm 0.26$. The errors in brightness are calculated from MCMC averages over all the MCMC fits and from the uncertainty in the calibration relations.

There is a single magnified OGLE V -band observation at $t = 6896.50$ (HJD'), and this results in a relatively large, 10% uncertainty in the V -band source flux for the best fit model. As a result, the OGLE VI source colors given a source star color of $V - I = 1.45 \pm 0.11$. The color of the source star is bluer than the average main sequence star color as can be seen in figure 4. Because we have only this single V -band measurement, we also calculate the source star color from MOA-Red and OGLE- I band following Gould et al. (2010a) and Bennett et al. (2012). Since we have a large number of MOA-Red and OGLE- I observations when the source is significantly magnified, we expect a robust measurement of the $R_{\text{MOA}} - I$ source color. About 140 bright, isolated stars with I -band magnitude $I < 16$ and $1.0 < V - I < 2.6$ are matched between the MOA-II and OGLE III reference images, and we used these to find the following calibration relation:

$$R_{\text{MOA}} - I_{\text{OGLEIII}} = 0.18143 \times (V - I)_{\text{OGLEIII}},$$

where the R_{MOA} passband has been calibrated to give $R_{\text{MOA}} = I_{\text{OGLEIII}}$ when $(V - I)_{\text{OGLEIII}} = 0$. The RMS error for this calibration relation is 0.0343, for a formal uncertainty of $0.0343/\sqrt{N} = 0.0029$, but we assume a calibration uncertainty of 0.02 for $R_{\text{MOA}} - I_{\text{OGLEIII}}$.

Our models give a source brightnesses of $I_S = 19.07 \pm 0.14$ and $R_{\text{MOA},S} = 19.34 \pm 0.15$ and a calibrated source color of $V - I = 1.52 \pm 0.11$. This color is less than $1-\sigma$ away from the color of the source derived from OGLE V -band data, so we conclude that the blue color from the OGLE data is probably real. However, the average color from both measurements is $V - I = 1.48 \pm 0.08$, which still has a relatively large error bar. We take this average as the correct color of the source. This color is plotted in blue point in the color magnitude diagram of all stars within $140''$ of the source star, Figure 4. The green points in the CMD figure 4 show the HST CMD plot (Holtzman et al. 1998) shifted to have the same red clump centroid position as the OGLE-III stars. The source color is slightly bluer than the main sequence star distribution shown with green points in the HST CMD in figure 4. The average color of main sequence bulge stars in the same magnitude range of the source ($I = 19.07 \pm 0.14$) in the HST CMD is $V - I = 1.75$. We can estimate the probability that a star with the measured color of the source ($V - I = 1.48 \pm 0.08$) is drawn from this HST distribution by integrating the Gaussian describing the measured source color with its error bar over the distribution of stars in the same magnitude range from the HST CMD. We then divide this result by the result of the integral with the same error bar, but centered on the average color of $V - I = 1.75$. The ratio of integral centered on the measured color and the integral centered on

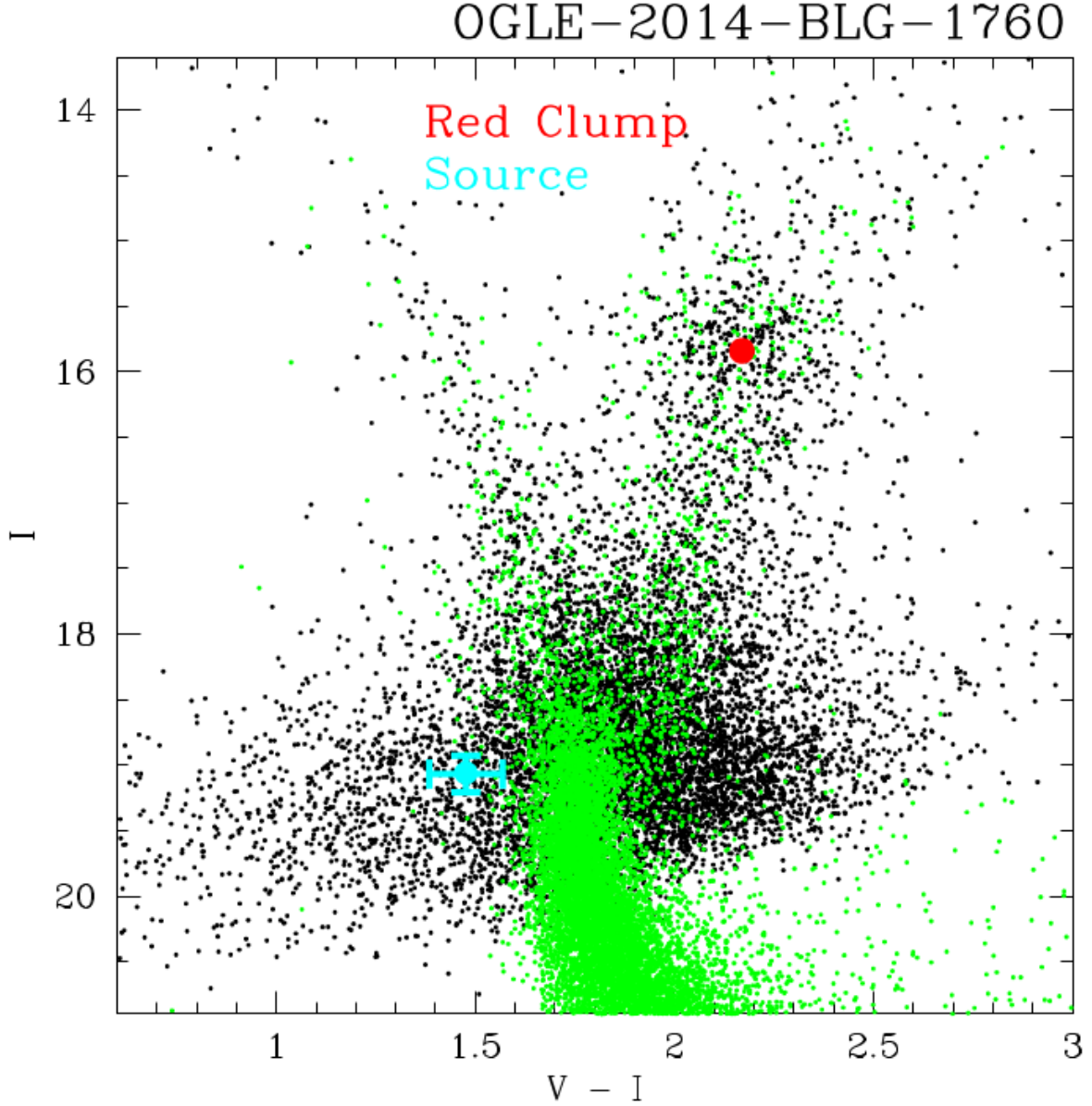


Fig. 4.— The $(V - I, I)$ color magnitude diagram (CMD) of the stars in the OGLE-III catalog Szymański et al. (2011) within $140''$ of OGLE-2014-BLG-1760. The red spot indicates red clump centroid, and the cyan spot indicates the source magnitude and color with error bars. The green points show HST CMD of Baade’s window transformed to have the same red clump centroid as this field. The source star is slightly bluer than the HST main sequence stars. This might be explained by a young, blue source in the Milky Way disk on the far side of the bulge.

the average color is 0.05, indicating that this source color is marginally consistent with being drawn from the known bulge star population. With nearly, 50 planetary microlensing events published to date, we would expect one or two to be found with such a blue source star. On the other hand, it is also possible that blue stars are preferentially lensed because they are at a greater distance. This can be the case if the source is a young blue (late A or early F) star on the far side of the Galactic disk, assuming negligible extinction beyond the bulge on this line-of-sight. Such stars would have a much larger microlensing event rate, so they could be preferentially lensed by bulge stars. On the other hand, it is possible that the CMD in this field is noticeably different than that of Baade’s window where the Holtzman et al. (1998) image was taken.

We calculate the extinction in the direction of the source using the method described by Bennett et al. (2014). The position of the centroid of red clump in the OGLE III catalog is found to be $(V - I, I)_{\text{RC}} = (2.20, 15.84)$ as shown in figure 4. From Bensby et al. (2011) and Nataf et al. (2013), the dereddened red clump centroid is determined to be $(V - I, I)_{\text{RC}} = (1.06, 14.39)$. Hence, the extinction at this galactic coordinate is : $(E(V - I), A_I)_{\text{RC}} = (1.14, 1.45)$. The extinction to the source star is assumed to be same as the average extinction for the red clump stars within $140''$ since most of the extinction is thought to be in the foreground. Thus, the extinction corrected source color and brightness are $(V - I, I)_{\text{S},0} = (0.34, 17.62)$, as shown in blue in figure 4.

The source radius is calculated from the dereddened source magnitude and color using the following formula, obtained from a private communication with Tabettha Boyajian:

$$\log_{10}(2\theta_*) = 0.50141358 + 0.41968496(V - I) - 0.2I \quad (5)$$

For the source color or $V - I = 1.48$, the calculated source radius is $\theta_* = (6.57 \pm 0.11) \times 10^{-4}$ mas. The relative proper motion and Einstein radius are calculated from:

$$\mu_{\text{rel}} = \frac{\theta_*}{t_*} \quad (6)$$

$$\theta_E = \theta_* \times \frac{t_E}{t_*} \quad (7)$$

Since the best fit model has $t_E = 15.87$ days and $t_* = 0.04$ days, we find:

$$\mu_{\text{rel}} = 6.55 \pm 1.12 \text{ mas/yr} \quad (8)$$

$$\theta_E = 0.29 \pm 0.05 \text{ mas} . \quad (9)$$

There is a 5% uncertainty in source radius relation (equation 5). We assume 1-2% error in the calibration relations (equations 3 and 4).

5. Lens Properties and Discussion

If we assume a standard Galactic model (Bennett et al. 2014) with a source star in the bulge and we assume that all stars and brown dwarf have an equal probability of hosting a planet with

the measured properties, then we can perform a Bayesian analysis to estimate the lens system properties. We ran an MCMC run with about 180,000 links to obtain the *posterior* distributions presented in Table 3 and Figure 5. The mass of the host star is only approximately determined to be $M_* = 0.51^{+0.44}_{-0.28} M_\odot$, so it could be an M, K, or G star. The 1-sigma range of the planet mass, $m_p = 182^{+137}_{-83}$ spans the range from the mass of Saturn to that of Jupiter. The distance to the lens system is more precisely determined, due to the relatively small angular Einstein radius, $\theta_E = 0.29 \pm 0.05$ mas. Our analysis predicts a lens system distance of $D_L = 6.86 \pm 1.11$. This implies that the lens system is very likely to be in the Galactic bulge.

Penny et al. (2016) argue that the published planetary microlensing events show a dearth of planets orbiting Galactic bulge stars. This OGLE-2014-BLG-1760L lens system would seem to be a counterexample, along with a number of other planetary microlens systems, such as OGLE-2005-BLG-380L (Beaulieu et al. 2006), OGLE-2008-BLG-092L (Poleski et al. 2014), MOA-2008-BLG-310L (Janczak et al. 2010), OGLE-2008-BLG-355L (Koshimoto et al. 2014), MOA-2011-BLG-353L (Rattenbury et al. 2015) and MOA-2011-BLG-293L (Yee et al. 2012; Batista et al. 2014). Actually, the problem with the Penny et al. (2016) analysis is pretty easy to understand. The Einstein radius crossing times (t_E) for bulge events are significantly smaller than the t_E values for disk events, but the detection efficiencies for microlensing events and planetary signals are substantially higher for events with large t_E values. The statistical analysis of Suzuki et al. (2016) shows that the planet detection efficiency weighted median t_E value is ≈ 42 days. This effect occurs for high magnification events (Gould et al. 2010b) because high magnification is much easier to predict when t_E is large, and for low magnification events (Suzuki et al. 2016) because the planetary signal duration (for fixed q) is proportional to t_E . This effect can be accounted for with accurate detection efficiency calculations, but Penny et al. (2016) use a detection efficiency calculation for an advance ground-based survey, that is much more sensitive than any ground-based survey undertaken to date. One of us (Bennett 2004) has previously studied a variety of ground-based microlensing surveys with a wide range of telescope options, and these simulations show that this detection efficiency bias

Table 3. Lens System Parameters

parameter	units	$(V - I)_S = 1.48 \pm 0.08$
Host star mass, M_*	M_\odot	$0.51^{+0.44}_{-0.28}$
Planet mass, m_p	M_\oplus	182^{+137}_{-83}
Host star - Planet 2D separation, a_\perp	AU	$1.75^{+0.34}_{-0.33}$
Host star - Planet 3D separation, a_{3D}	AU	$2.57^{+1.12}_{-0.45}$
Lens distance, D_L	kpc	6.86 ± 1.11
Lens magnitude, I_{Lens}	Cousins I	$23.42^{+1.89}_{-2.92}$
Lens magnitude, H_{Lens}	H	$20.80^{+1.54}_{-2.31}$

with t_E is much stronger with the less capable surveys that can approximate the sensitivity of the observing programs that have discovered the published events.

It should also be noted that the color of the source star $V - I = 1.48 \pm 0.08$ implies that this star is bluer than and only marginally consistent with bulge main sequence shown in Figure 4. This source star could be a "blue straggler" which is an old, bright blue star that probably formed from a merger of two smaller stars, but these stars are rare, or it could be that this field has a larger fraction of bluer, metal poor stars than the HST Baade's window stars plotted in Figure 4. But this also seems unlikely. Another possibility is that this star is a relatively young blue star that resides in the Galactic disk on the far side of the bulge with minimal additional extinction between the bulge and this source star. If so, HST observations taken separated by 2 years could reveal the characteristic source star proper motion of a far side disk star. Since the galactic coordinates of the source, $(l, b) = 1.3186, -2.2746$ are pretty close to the nominal WFIRST exoplanet microlensing survey fields (Spergel et al. 2015) field, so understanding the source distance distribution in this area of the bulge is important for WFIRST.

The probability distribution for the brightness of the lens star in I and H -bands is shown in Figure 6. The blend magnitude from best fit is found $I_{bl} = 17.94$ which is brighter than the lens star magnitude predicted in Table 3 and Figure 6. Since the lens-source relative proper motion is $\mu_{rel} = 6.55 \pm 1.12$ mas/yr, the source and lens will be separated by ~ 1 HST pixel (39.6 ± 6.2) by 2020. If the lens system is observed directly in high resolution images, then the brightness measurement of lens leads to the precise calculation of the mass and distance to the lens system (Bennett et al. 2006, 2015; Batista et al. 2015). But in the I -band, the source star is brighter than the median prediction for the lens by ~ 4 magnitudes (see Figure 6), which makes it difficult to observe the lens in I band with the high resolution follow-up images unless the lens and source are completely resolved. The extinction corrected ($I - H$) color of the source is obtained from ($V - I$) color using Kenyon & Hartmann (1995). The H -band extinction A_H is also obtained from A_I and A_V using the Cardelli et al. (1989) formula. From the I -band magnitude, the ($I - H$) color and the H -band extinction, A_H , the H -band magnitude of the source is calculated to be $H_S = 17.96$. From Figure 6, we see that the H -band magnitudes of source and median prediction for the lens differ by ~ 2.0 - 2.5 magnitude. The uncertainty in the source brightness is measured from the Markov chain links. We also include the uncertainty in the source color and magnitude. There is 5% uncertainty in the color conversion from the extinction corrected ($V - I$) to ($I - H$). The red lines in Figure 6 is such that if lens is at least as bright as the red lines (*i.e.* it lies in the red-shaded region) then lens+source brightness is brighter than the $3\text{-}\sigma$ upper limit on the source brightness. This would mean that the lens could be detected when it is still unresolved from the source. Since most of the lens flux histogram lies to the right of the red-shaded region, the lens is likely to be too faint to be detected in high resolution images unless lens and source are partially resolved. Since the relative lens-source proper motion, $\mu_{rel} \sim 6.5$ mas/yr, the lens and source are expected to be resolvable by JWST, HST or adaptive optics imaging some in 6-8 years after peak magnification, in 2020 - 2022.

Suzuki et al. (2016) derived a mass ratio function from planets detected in MOA-II survey

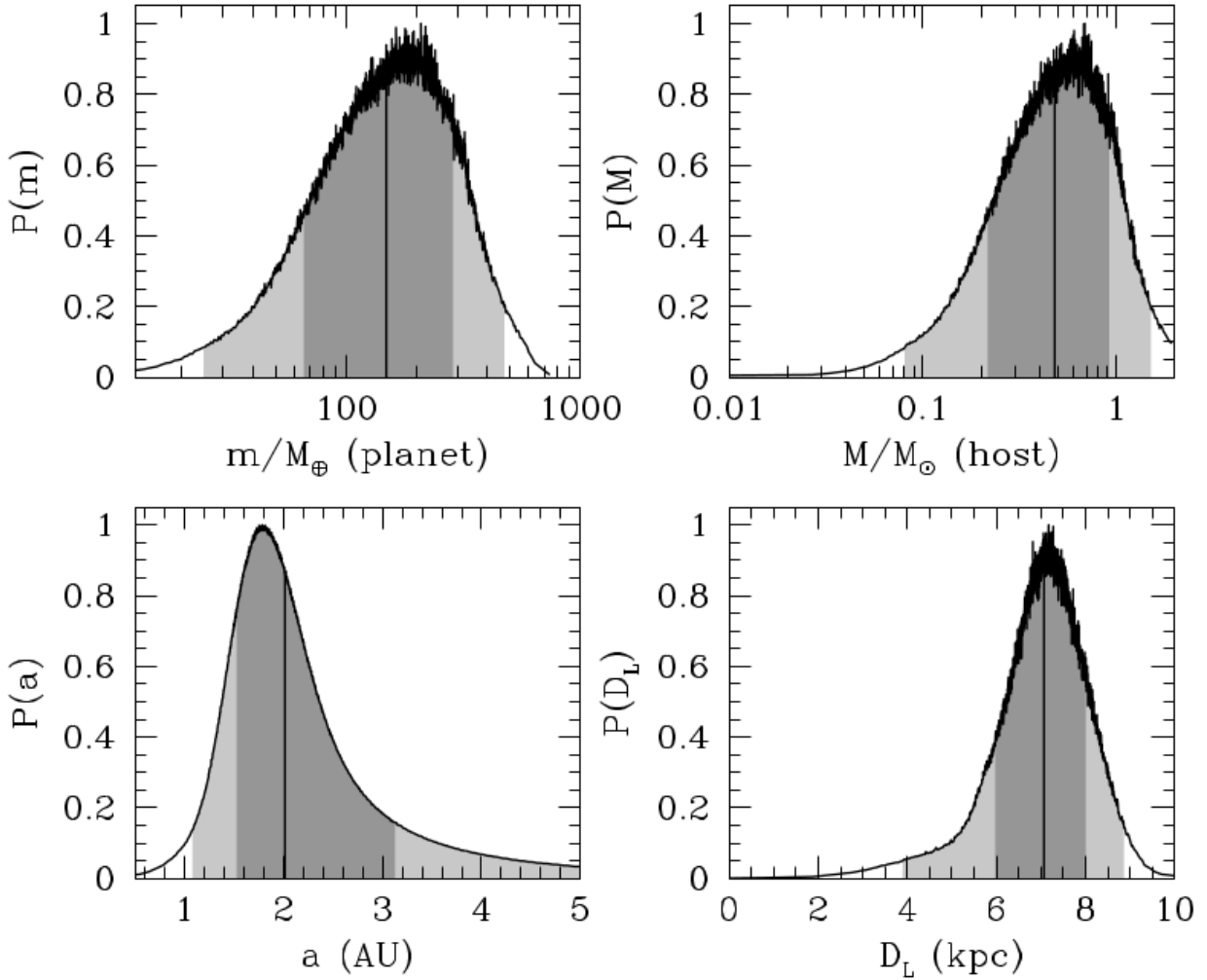


Fig. 5.— The probability distribution of planet mass, host star mass, planet - host star separation and distance to lens system, derived using Bayesian statistical analysis. The central 68.3% of the distribution is shaded dark grey and the remaining central 95.4% of the distribution is shaded light grey. The vertical black line marks the median of the probability distribution of respective parameters.

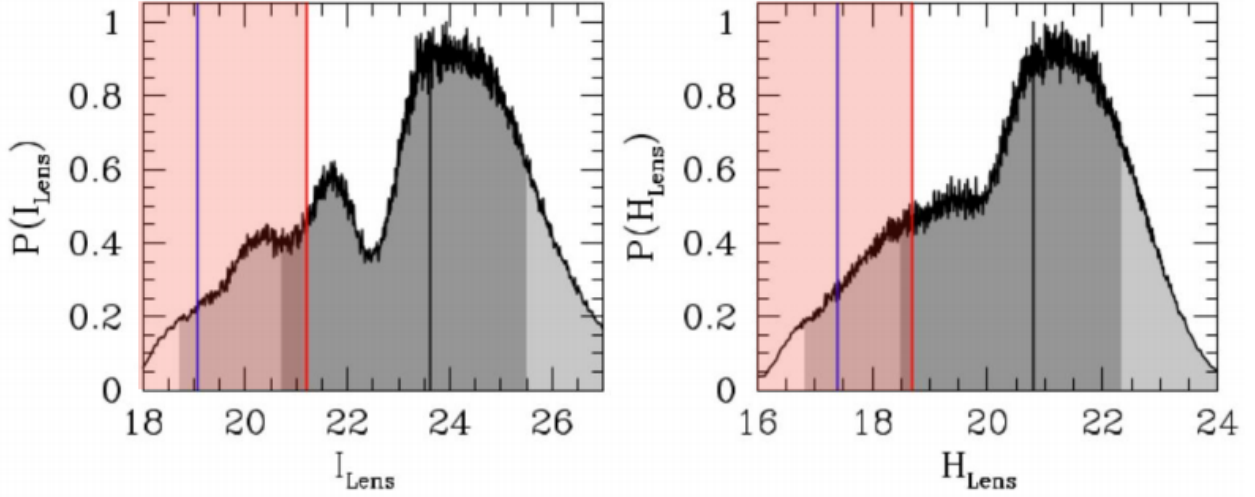


Fig. 6.— The probability distribution for the I and H -band lens star magnitudes given the source radius estimate based on the source magnitude and color given in Figure 4. As in Figure 5, central 68.3% is shaded dark grey and the remaining central 95.4% of the distribution is shaded light grey. The blue lines indicate the source magnitude, and the left and right panels show the I and H magnitude distributions, respectively. The vertical red lines mark the lens brightness corresponding to the $3\text{-}\sigma$ upper limit on the source brightness, so if the lens is in the light red shaded region it will be bright enough to push the combined lens+source brightness above the brightness from the light curve models. In this case, the excess brightness from the lens will be detectable even when the lens and source remain unresolved. If the lens is fainter and located to the right of the red shaded region, we will not be able to identify the lens with high angular resolution JWST, HST or adaptive optics observations until the lens star begins to separate from the source 5-8 years after peak magnification.

data, and discovered a break in the mass ratio function at $q \sim 10^{-4}$. The OGLE-2014-BLG-1760Lb planetary mass ratio of $q = 8.6 \pm 0.9$ is above the mass ratio break $q_{br} \sim 10^{-4}$. This is close to Jupiter’s mass ratio, but the host star probably has a mass of $M_* \lesssim M_\odot$, so this planet is probably a low-mass gas giant, like Saturn. Follow up observations with JWST, HST or adaptive optics in 2020-2022 should be able to measure the lens brightness and determine the planetary mass and distance using the methods of Bennett et al. (2006, 2007, 2015) and Batista et al. (2015). Later with WFIRST (Spergel et al. 2015), a similar kind of study will provide the statistics needed to determine the planetary mass function as a function of the host star mass and distance.

A.B., D.P.B. and D.S. were supported by NASA through grants NASA-NNX12AF54G and NNX13AF64G. I.A.B. and P.Y. were supported by the Marsden Fund of Royal Society of New Zealand, contract no. MAU1104. N.J.R. was supported through Royal Society of New Zealand Rutherford Discovery Fellowship. A.S, M.L. and M.D. were supported through Royal Society of New Zealand. T.S. received support from JSPS23103002, JSPS24253004 and JSPS26247023. MOA project received grants from JSPS25103508 and 23340064. A.F. was supported by the Astrobiology Project of the Center for Novel Science Initiatives (CNSI), National Institutes of Natural Sciences (NINS) (Grant Number AB261005). The OGLE project received funding from National Science Centre, Poland, grant MAESTRO 2014/14/A/ST9/00121 to AU. OGLE team thanks Profs. M. Kubiak and G. Pietrzyński, former members of the OGLE team, for their contribution to the collection of the OGLE photometric data over the past years. DMB was supported by NPRP grant X-019-1-006 from the Qatar National Research Fund (a member of Qatar Foundation). This work makes use of observations from the LCOGT network, which includes three SUPAscopes owned by the University of St Andrews. The RoboNet programme is an LCOGT Key Project using time allocations from the University of St Andrews, LCOGT and the University of Heidelberg together with time on the Liverpool Telescope through the Science and Technology Facilities Council (STFC), UK. This research has made use of the LCOGT Archive, which is operated by the California Institute of Technology, under contract with the Las Cumbres Observatory. We thank Prof. Andrew Gould and μ FUN team for allowing us to use their data and acknowledge their hard work and contribution in collecting the μ FUN data.

REFERENCES

- Alard C., 2000, *A&AS*, 144, 363
- Alard C., Lupton R. H., 1998, *ApJ*, 503, 325
- Albrow, M.D., et al., 2009, *MNRAS*, 397, 2099
- Alcock, C., et. al., 1995, *ApJ*, 454, 125

- Batista, V., Beaulieu, J.-P., Bennett, D.P., et al., 2015, *ApJ*, 808, 170
- Batista, V., Beaulieu, J.-P., Gould, A., et al. 2014, *ApJ*, 780, 54
- Beaulieu, J.-P., Bennett, D. P., Fouqué, P., et al. 2006, *Nature*, 439, 437
- Bennett, D. P. 2004, *Extrasolar Planets: Today and Tomorrow*, 321, 59 (arXiv:astro-ph/0404075)
- Bennett, D. P., 2010, *ApJ*, 716, 1408
- Bennett, D. P. & Rhie, S. H., 1996, *ApJ*, 472, 660
- Bennett, D. P., Anderson, J., et al., 2006, *ApJ*, 647, L171
- Bennett, D. P., Anderson, J., 2007, Gaudi, S. B., *ApJ*, 660, 781
- Bennett, D. P., Rhie, S., et al., 2010, *ApJ*, 713, 837
- Bennett, D. P., Sumi, T., Bond, I. A., et al., 2012, *ApJ*, 757, 119B
- Bennett, D. P., Batista, V., Bond, I. A., et al., 2014, *ApJ*, 785, 155
- Bennett, D. P., Bhattacharya, A., Anderson J., et al., 2015, *ApJ*, 808, 169B
- Bensby, T., Adén, D., Melendez, J., et al., 2011, *A&A*, 533, A134
- Bessell, M. S. & Brett, J. M., 1988, *PASP*, 100, 1134
- Bond, I. A., Abe, F., Dodd, R. J., et al., 2001, *MNRAS*, 327, 868
- Bramich, D. M., 2008, *MNRAS*, 386, L77b
- Cardelli, J. A., Clayton G. C., & Mathis J. A., 1989, *ApJ*, 345, 245C
- Claret, A., 2000, *A&A*, 363, 1081C
- Gaudi, S., Bennett, D. P., Udalski, A., et al., 2008, *Science*, 319, 927
- Gould, A., 1992, *ApJ*, 392, 442
- Gould, A., Loeb, A., 1992, *ApJ*, 396, 104G
- Gould, A., Dong, S., Bennett, D. P., et al. 2010a, *ApJ*, 710, 1800
- Gould, A., Dong, S., Gaudi, B.S., et al. 2010b, *ApJ*, 720, 1073
- Han, C., Bennett, D.P., Udalski, A., et al., 2016, *ApJ*, submitted
- Holtzman, J. A., Watson, A. M., Baum, W. A., et al., 1998, *ApJ*, 115, 1946H
- Ida, S., & Lin, D. N. C., 2005, *ApJ*, 626, 1045

- Janczak, J., et al., 2010, *ApJ*, 711, 731
- Kennedy, G. M., Kenyon, S. J., & Bromley, B. C., 2006, *ApJL*, 650, L139
- Kenyon, S. J., & Hartmann, L., 1995, *ApJSS*, 101, 117
- Koshimoto, N., Udalski, A., Sumi, T., et al. 2014, *ApJ*, 788, 128
- Lecar, M., Podolak, M., Sasselov, D., & Chiang, E, 2006, *ApJ*, 640, 1115
- Lissauer, J.J. 1993, *Ann. Rev. Astron. Ast.*, 31, 129
- Mao, S., Paczyński, B., 1991, *ApJ*, 374L, 37M
- Muraki, Y., et al., 2011, *ApJ*, 741, 22
- Nataf, D. M., Gould, A., Fouqué, P., et al., 2013, *ApJ*, 769, 88
- Penny, M., Henderson, C. B., Clanton, C., 2016, arXiv:1601.02807
- Paczyński, B., et al, 1986, *ApJ*, 304, 1P
- Poleski, R., Skowron, J., Udalski, A., et al. 2014, *ApJ*, 795, 42
- Rattenbury, N. J., Bennett, D. P., Sumi, T., et al. 2015, *MNRAS*, 454, 946
- Spergel, D., Gehrels, N., Baltay, C., et al. 2015, arXiv:1503.03757
- Smith, M. C., Mao, S. & Woźniak, P. R., 2002, *MNRAS*, 332, 962
- Sumi, T., Kamiya, K., Bennett, D. P., et al., 2011, *Nature*, 473, 349
- Suzuki, D., Bennett, D. P., Sumi, T., et al., 2016, *ApJ*, submitted.
- Szymański, M. K., Udalski, A., Soszyński, I., et al., 2011, *Acta Astron.*, 60, 295
- Szymański, M. K., Udalski, A., Soszyński, I., et al., 2011, *Acta Astron.*, 61, 83
- Tomany, A. B. & Crots, A. P., 1996, *AJ*, 112, 2872
- Udalski, A., 2003, *Acta Astron.*, 53, 291
- Udalski, A., Szymański, M., Kałużny, J., Kubiak, M., Mateo, M., Krzemiński, W., & Paczyński, B. 1994, *Acta Astron.*, 44, 227
- Udalski, A., Szymański, M. K., & Szymański, G., 2015, *Acta Astron.*, 65, 1
- Verde, L., Reiris, H. V., & Spergel, D. N., 2003, *ApJS*, 148, 195
- Wozniak P. R., 2000, *Acta Astron.*, 50, 421

Yee, J. et al., 2012, ApJ, 755, 102